AGU PUBLICATIONS

JGR

Journal of Geophysical Research: Earth Surface

RESEARCH ARTICLE
10.1002/2017JF004364

Key Points:
- Presence of secondary basins causes nearby channels to form farther away from the bank of the estuary
- Closure of a secondary basin causes lateral displacement of the nearby channel toward the bank
- Model outcomes are in qualitative agreement with observations in the Western Scheldt Estuary

Supporting Information:
- Supporting Information S1

Correspondence to:
A. Nnafie,
abnnafie@gmail.com

Citation:
Nnafie, A., Van Oyen, T., De Maerschalck, B., van der Vegt, M., & van der Wegen, M. (2018). Estuarine channel evolution in response to closure of secondary basins: An observational and morphodynamic modeling study of the Western Scheldt Estuary. *Journal of Geophysical Research: Earth Surface*, *123*. https://doi.org/10.1002/2017JF004364

Received 17 MAY 2017
Accepted 20 DEC 2017
Accepted article online 3 JAN 2018

Estuarine Channel Evolution in Response to Closure of Secondary Basins: An Observational and Morphodynamic Modeling Study of the Western Scheldt Estuary

A. Nnafie[1,2], T. Van Oyen[1], B. De Maerschalck[1], M. van der Vegt[2], and M. van der Wegen[3,4]

[1]Flanders Hydraulics Research, Antwerp, Belgium, [2]IMAU, Utrecht University, Utrecht, Netherlands, [3]IHE, Delft, Netherlands, [4]Deltares, Delft, Netherlands

Abstract The fringes of estuaries are often characterized by the presence of side embayments (secondary basins), with dimensions in the order of hundreds of meters to tens of kilometers. The presence of secondary basins significantly alters the hydrodynamic and sediment characteristics in the main estuary, implying that loss of secondary basin area due to human interventions might affect the estuarine morphodynamics. Analysis of historical bathymetric data of the Western Scheldt Estuary (Netherlands) suggests that closure of its secondary basins has triggered the observed lateral displacement of the nearby channels. This analysis motivated investigation of the impact of secondary basins on decadal evolution of estuarine channels, using the numerical model Delft3D. Model results show that channels that form near a secondary basin are located farther away from the bank of the estuary with respect to their positions in the case without a basin. Overall, results in cases with two or three basins are similar to those in case with one single basin. The wider the basin, the farther away the nearby channel forms. Removing a secondary basin causes a lateral displacement of the nearby channel toward the bank, indicating that the observed lateral displacement of channels in the Western Scheldt is triggered by closure of its secondary basins. The physical explanation is that tidal currents in the main estuary are weaker and more rotary near secondary basins, favoring sediment deposition and shoal development at these locations. Model results are particularly relevant for estuaries with moderate to high friction and converging width.

1. Introduction

Many existing estuaries were formed during the rapid sea level rise in the early Holocene when existing paleo-valleys flooded during the postglacial sea level rise (Dalrymple et al., 1992; Schubel & Pritchard, 1972). Side embayments appeared along the fringes of many estuaries, resulting from the drowning of (1) paleo-valleys (Dabrio et al., 2000; Fletcher et al., 1992; Perillo, 1995; Woodruff et al., 2013; Yellen et al., 2017) or (2) coastal plains that experienced major human-induced subsidence due to intensified agriculture use of peat areas (Pierik et al., 2017; Syvitski et al., 2009; Törnqvist et al., 2008). After the formation of these estuarine systems, the interplay between sea level rise, sediment availability, and sediment distribution by waves, tides, and rivers determined their subsequent morphological development (Pierik et al., 2017; Pye & Blott, 2014; Rossi et al., 2011). Examples of estuaries with side embayments include the Shannon Estuary (Ireland), Solway Firth Estuary (UK), Colombia River Estuary (USA), Dart Estuary (UK), Ems Estuary (Dutch-German border), Gulf of Ob Estuary (Russia), Salmon River Estuary (Canada), Miramichi River estuary (Canada), Potomac River estuary (USA), and Connecticut River estuary (USA). Maps of some of these estuaries are shown in Figure 1. The side embayments are typically hundreds to thousands of meters wide and hundreds of meters to tens of kilometers long. Note that, in the literature, side embayments are also referred to as bays (Sherwood et al., 1990), tributary valleys (Dalrymple et al., 1992), off-river coves (Woodruff et al., 2013; Yellen et al., 2017), branching or secondary channels (Alebregtse & de Swart, 2014), etc. In this study, following Roos and Schuttelaars (2015), these side embayments are referred to as secondary basins.

In the last centuries, planforms (i.e., geometric shape in plane view) of many estuaries drastically changed as a result of increased human interventions such as diking, sand extraction, channel deepening, and land reclamations (French, 2002; Pye & Blott, 2014). These interventions caused a significant reduction in surface area

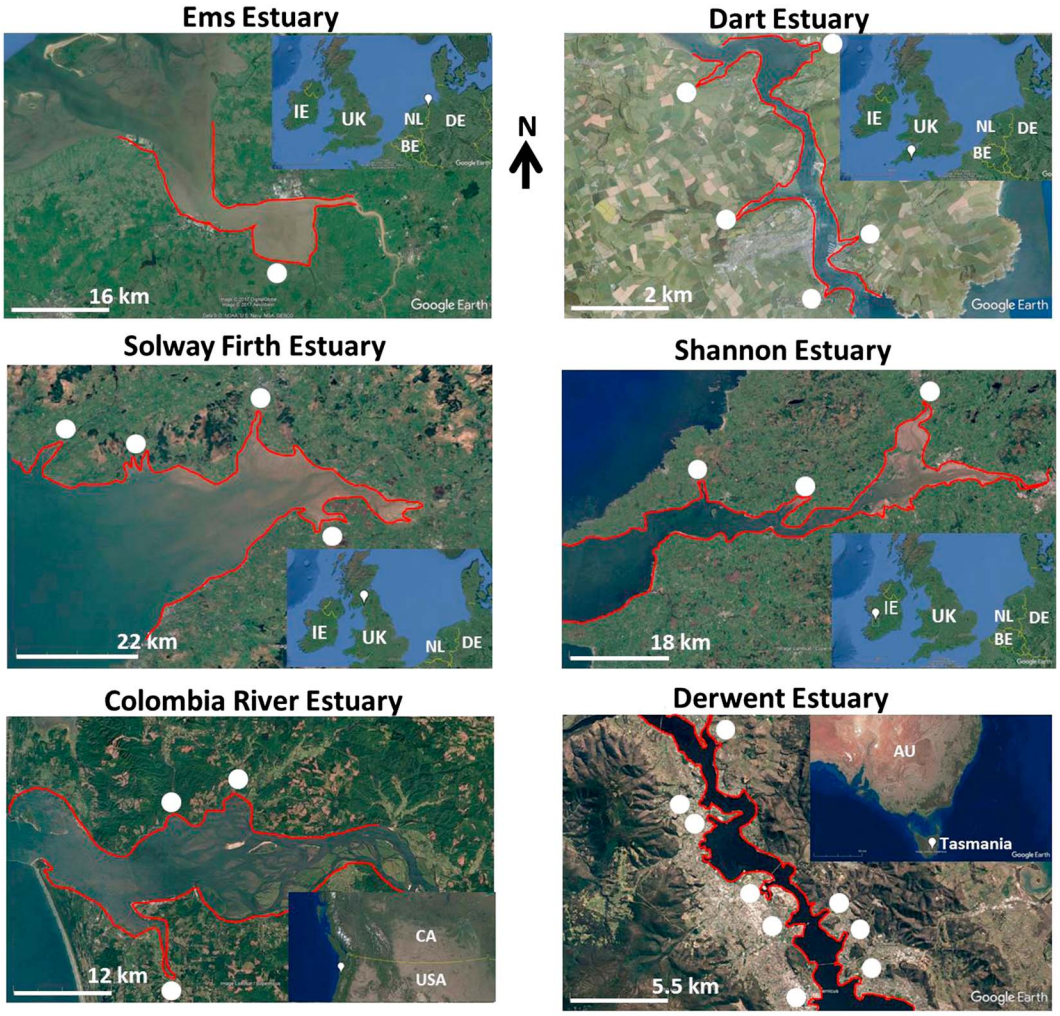

Figure 1. Maps showing examples of estuaries with secondary basins: Ems Estuary (Netherlands, Germany), Dart Estuary (UK), Solway Firth Estuary (UK), Shannon Estuary (Ireland), Colombia River Estuary (USA), and Derwent Estuary (Tasmania, Australia). White placemarks in the overview maps indicate locations of the estuaries. White dots mark some examples of secondary basins that are located along the estuary margins. Red lines indicate the approximate positions of the estuary banks.

of secondary basins, either directly through diking and filling activities or indirectly through increased sediment supply from the main estuary after a major intervention. For example, based on the analysis of historical bathymetric surveys in the Colombia River Estuary (USA, Figure 1), Sherwood et al. (1990) found that particularly estuarine intertidal and supratidal surface areas (including secondary basin area) greatly reduced at the end of the nineteenth and beginning of the twentieth century, which they attributed to the human activities that took place in this estuary (constructing of jetties, channel dredging, diking, and filling activities). Another example is the San Francisco Estuary, where some secondary basins that used to exist in 1856 had filled and disappeared completely in the subsequent time period, as a result of high sediment delivery from the main estuary caused by the hydraulic gold mining activities that started in the 1850s (Jaffe et al., 2007). Other examples are the Ems, Shannon, and Western Scheldt Estuaries, where land reclamations in the last two centuries resulted in a significant reduction in their secondary basin areas (Healy & Hickey, 2002; Van Maren et al., 2016). In the case of the Western Scheldt Estuary, these reclamations even led to the entire closure of its secondary basins (Van der Spek, 1997; Zitman, 1999).

Secondary basins are usually low energy environments compared with the high energetic main estuary, and therefore, they provide the vertical accommodation space necessary to trap sediment and reduce the net sediment delivery to the ocean (Van Maren et al., 2016; Woodruff et al., 2013; Yellen et al., 2017). A reduction

in secondary basin area due to human interventions will likely influence the entire estuarine sand budget and morphodynamics. Moreover, secondary basins are important sinks for nutrients, implying that reduction in secondary basin area will have ecological implications as well, such as a decline in phytoplankton and mussel population (Archambault et al., 1999). Furthermore, the presence of secondary basins has a major impact on the tidal characteristics and sediment transport in the main estuary (Alebregtse & de Swart, 2014; Kumar et al., 2014; Li et al., 2016), meaning that reduction of the basin area will likely affect the hydrodynamic and sediment processes in the estuary. For example, the decreasing area of a secondary basin in the Ems Estuary, and the resulting loss in accommodation space for sediment storage in this basin, likely led to the observed increase of the estuarine turbidity maximum (ETM) in this estuary (Van Maren et al., 2016; Yellen et al., 2017). Reduction in the surface area (including secondary basin area) around the Shannon Estuary margin is believed to have significantly affected the sedimentary and morphodynamic processes within this estuary (Healy & Hickey, 2002). Finally, the closure of the secondary basins of the Western Scheldt Estuary (Figure 2) is believed to have greatly influenced the morphological evolution of this estuary over the last two centuries (see section 2.2).

Due to increased popularity among coastal managers to open new secondary basins to reduce tidal range and turbidity (Donner et al., 2012), various modeling studies have been conducted in the past few years to increase insight into the impact of secondary basins on estuarine tidal characteristics and sediment transport (Alebregtse & de Swart, 2014; Alebregtse et al., 2013; Kumar et al., 2014; Li et al., 2016; Roos & Schuttelaars, 2015). Besides the first analytical model to study the exchange of substances between secondary basins and the main estuary proposed by Okubo (1973), there have been no systematic studies on the effects of secondary basins on the estuarine hydrodynamics and sediment transport prior to 2013. Although these studies greatly increased understanding of the impact of secondary basins on the hydrodynamics and sediment transport in the main estuary (see section 5), knowledge of how these basins affect the long-term evolution (order of tens to hundreds of years) of the main estuary is still lacking. A recent analysis of bar characteristics in 25 estuaries by Leuven et al. (2017) showed that larger bars form at locations where the estuary is wider or secondary basins are present, suggesting that a reduction in secondary basin area would decrease the bar dimensions in the vicinity of the basin. In view of the reduction in surface area of secondary basins in many estuaries by human activities, there is a strong need to increase fundamental knowledge of the impact of secondary basins on the morphodynamic evolution of the main estuary. In addition, this knowledge will provide a first estimate of the potential morphodynamic impact of openings of new secondary basins on the main estuary.

This work addresses the effects of closure of secondary basins on the morphological evolution of the main estuary, which is motivated by analysis of historical bathymetric maps of the Western Scheldt Estuary (Figure 2a). In this estuary, multiple secondary basins used to exist in 1800 (Sloe, Braakman, and Hellegat; Figure 2b), which have been gradually reclaimed during the last two centuries (Van der Spek, 1997). Based on this analysis, it is hypothesized that the closure of these basins has triggered the observed lateral displacement of the nearby main channel toward the bank of the estuary.

The specific objectives are threefold. The first is to investigate the relative effects of the presence of a secondary basin on the long-term evolution (order decades to centuries) of estuarine channels compared to a case without such a basin. In particular, the effects of the presence of a secondary basin on the evolution of the nearby channel and the physical mechanisms underlying this evolution will be addressed. The second objective is to systematically quantify sensitivity of model results to the location, number, and geometry of secondary basins. To verify the hypothesis previously postulated, the third objective is to examine impact of removing a secondary basin on the evolution of the nearby channel. To this end, the state-of-the-art numerical model Delft3D (Lesser et al., 2004) is used, which has been successfully applied to morphodynamic modeling of estuaries and tidal basins (cf. Hibma et al., 2003; Van der Wegen & Roelvink, 2008). The Western Scheldt Estuary is selected as the study area, because of its large availability of bathymetric data since 1800, providing a great opportunity to compare model results with observations. It is important to stress that this study does not aim to hindcast the morphodynamic evolution of the Western Scheldt Estuary over the past two centuries, but rather to gain fundamental insight into the effects of secondary basins on estuarine morphodynamic evolution. Morphodynamic hindcasts of the Western Scheldt Estuary have already been the topic of the study by Dam et al. (2016).

This paper is organized as follows. In section 2, a description of the study area is given, including its hydrodynamic and sediment characteristics, as well as its morphological development between 1800 and present.

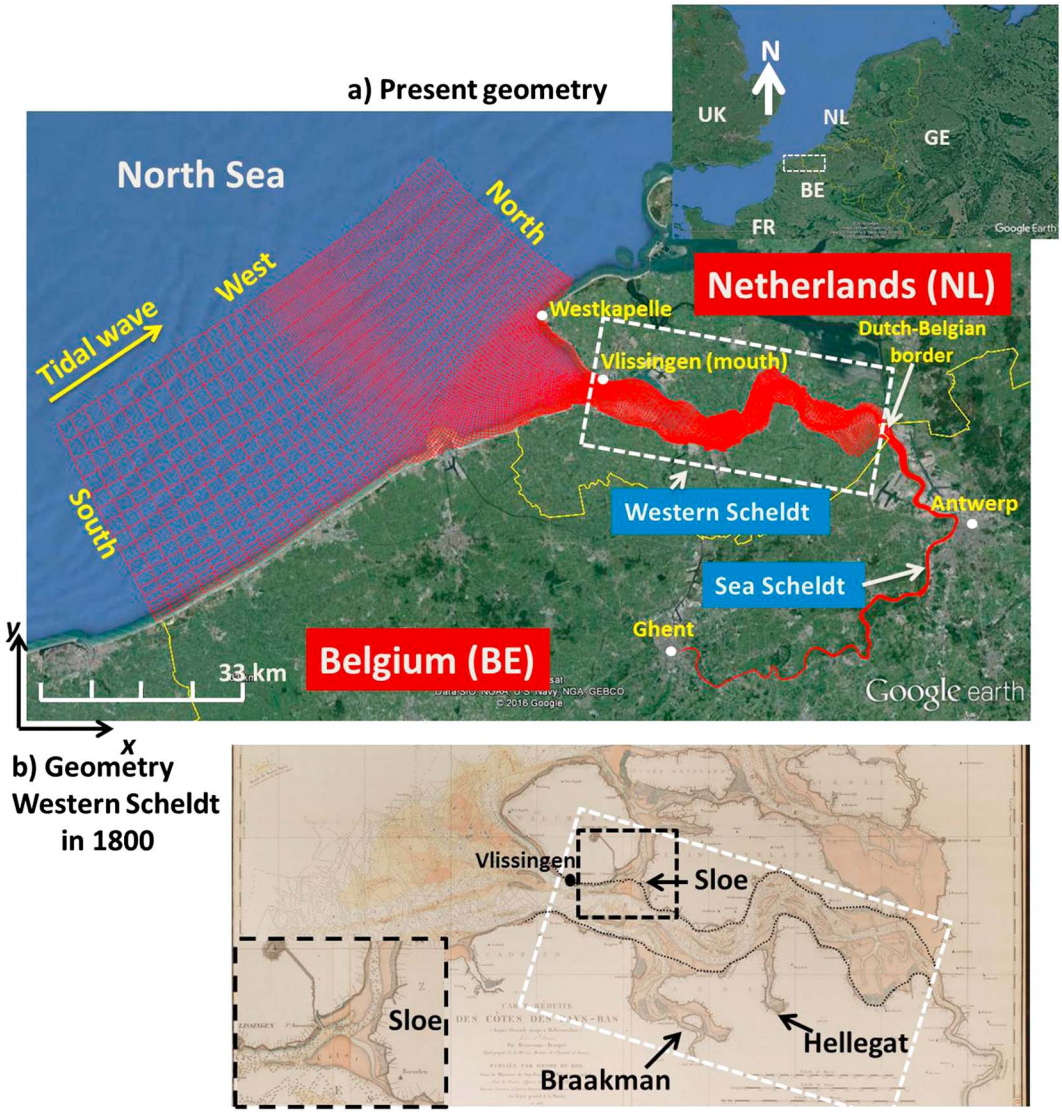

Figure 2. (a) Present-day geometric shape of the Western Scheldt Estuary (indicated by the white rectangle), which is the seaward of part of the Scheldt Estuary. Red lines display the used Delft3D computational grid, which covers the entire Scheldt Estuary and part of the North Sea. A Cartesian coordinate system is used with *x* and *y* pointing in eastern and northern directions, respectively. The yellow arrow indicates direction of the propagating tidal wave in the North Sea (south-north). (b) Geometrical shape of the Western Scheldt Estuary and its mouth in 1800 (Source: Department Maritime Access, The Government of Flanders). Arrows indicate former secondary basins Sloe, Braakman, and Hellegat. Shoals are represented by the orange colors. Black dotted lines denote the present-day geometric shape of the estuary. Insert on bottom left: enlargement of the Sloe basin.

Section 3 contains the model formulations and the setup of model experiments. Subsequently, in section 4, results from these experiments are presented, followed by a discussion (section 5). Finally, section 6 contains the conclusions.

2. Study Area

2.1. Present Morphology

The Western Scheldt is the seaward, marine part of the Scheldt Estuary (Figure 2a, indicated by the white rectangle), extending over ~ 60 km from Vlissingen (mouth) to the Dutch-Belgian border. The upper part of the Scheldt (called Scheldt River or Sea Scheldt) extends over ~ 100 km from the border to the city of Ghent. The present bathymetry of the Western Scheldt features a network of multiple channels, separated by elongated tidal flats (Figure 3a, bottom left). This channel network is characterized by relative short straight flood

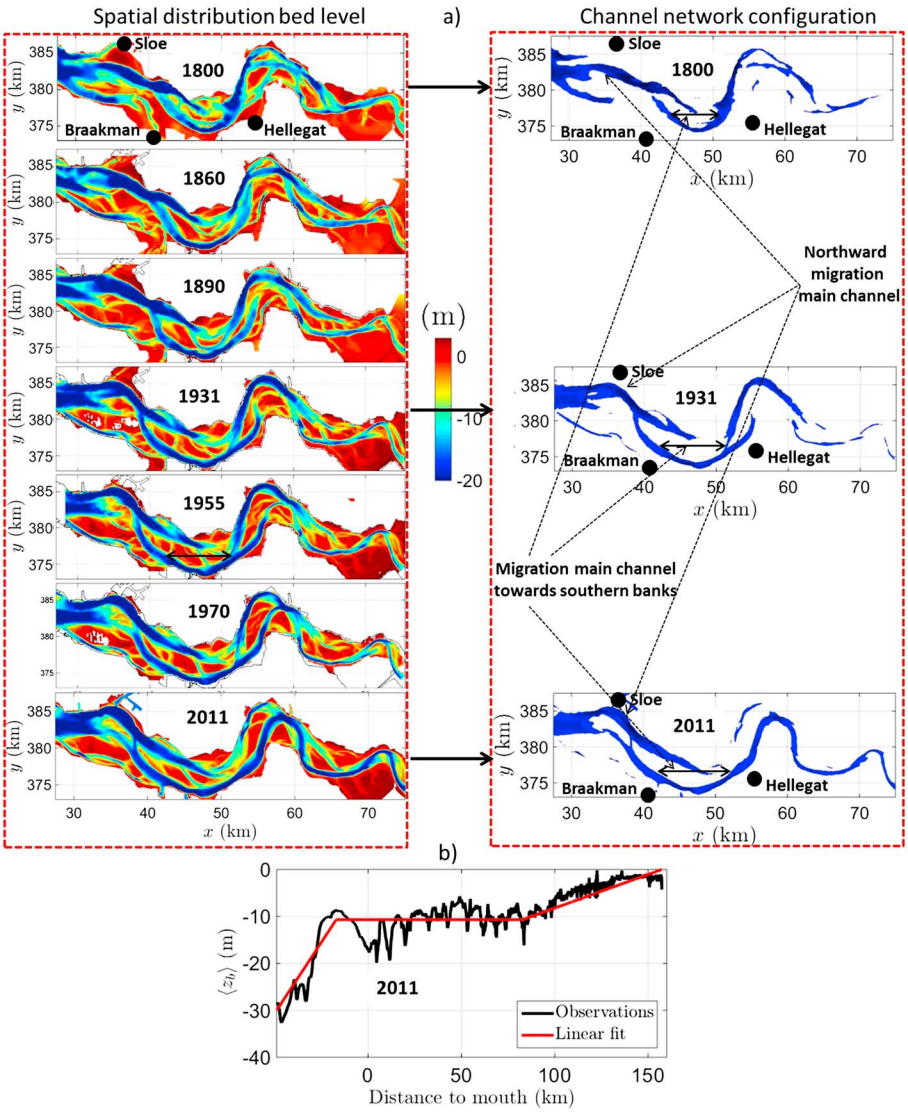

Figure 3. (a) (left column) Spatial distribution of the observed bed level z_b (in meters with respect to NAP, Dutch equivalent for mean sea level = MSL) of the Western Scheldt between 1800 and 2011. (right column) Plane view of channel network configurations ($z_b < -10$ m) in years 1800, 1931, and 2011. Dashed arrows indicate channel displacements toward the bank of the estuary where former secondary basins Sloe, Braakman, and Hellegat were located (denoted by black dots). (b) Width-averaged bed level $\langle z_b \rangle$ (black line) of the Scheldt Estuary in 2011 versus the long-channel distance with respect to mouth (Vlissingen). Red line is a piecewise linear fit to the data.

channels and meandering ebb channels (Jeuken, 2000; Van Veen, 1950). The width-averaged bed level $\langle z_b \rangle$ of the Western Scheldt (with respect to NAP, Dutch equivalent for mean sea level = MSL; $\langle \cdot \rangle$ denotes averaging over the width of the estuary) decreases from ~ 15 m at the mouth to ~ 7 m at its landward end (Figure 3b, black line). Further upstream, bed level $\langle z_b \rangle$ gradually decreases to ~ 3 m near Ghent. Lateral boundaries of the Western Scheldt Estuary are fixed by dikes and bank protection measures (Jeuken & Wang, 2010).

2.2. Historical Morphological Development

Loss of intertidal areas and closure of secondary tidal basins Sloe, Braakman, and Hellegat in the Western Scheldt Estuary, resulting from land reclamations, have considerably changed the geometric shape of the estuary over the last two centuries (Figure 2). Furthermore, Figure 3a (left and right columns) reveals that several large-scale bathymetric changes took place in the estuary between 1800 and 2011, including the lateral displacement of the meandering channel toward locations of former secondary basins Sloe, Braakman, and Hellegat (indicated by black dots). Near Sloe and Braakman, channel displacements were about 1.5 km and 2.5 km (Figure 4, blue circles), respectively, while the displacement near Hellegat (not shown) was ~1 km.

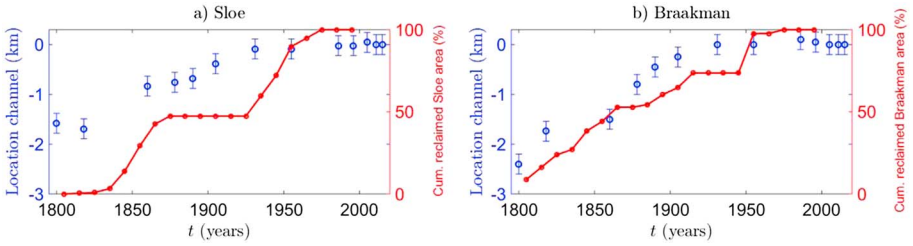

Figure 4. (a) Time evolution of the location of the main channel near Sloe (blue circles) with respect to its present location (2015) and of the cumulative reclaimed area of the Sloe basin (in percent, red line) between 1800 and 2015. Here channel location is estimated based on its maximum depth (with respect to MSL). Error bars of channel locations are also indicated. (b) As in Figure 4a, but for the location of the main channel near Braakman. Total reclaimed areas of Sloe and Braakman were $\sim 1.3 \cdot 10^7$ m^2 and $\sim 6.3 \cdot 10^7$ m^2, respectively. Data collected by Zitman (1999) were used to construct the red curves.

By plotting the cumulative total reclaimed area of basins Sloe and Braakman versus time using data from the study by Zitman (1999) (Figure 4, red lines), it appears that reduction of the Sloe and Braakman basin areas over time (Figures 4a and 4b, respectively) correlates well (with a correlation coefficient of 0.90 and 0.93, respectively) with the lateral displacement of the nearby channels (blue circles). Besides channel displacement, Figure 3a (right column) further shows that in the area of the strong estuary bend near Hellegat, the channel configuration underwent significant spatial changes between 1800 and 2011. In the beginning of the nineteenth century, this area used to consist of two channels. In the subsequent period, roughly between 1850 and 1950, this area was dominated by the presence of one main channel located along the northern bank. In the second half of the twentieth century, the southern channel became increasingly pronounced over time, resulting in the formation of a network of two main channels during this period. In the last two decades, a transition from a two-channel to a single-channel network took place, as a result of narrowing of the northern channel.

2.3. Hydrodynamic and Sediment Characteristics

The Scheldt Estuary is a mesotidal to macrotidal estuary in which the flow field is dominated by (semidiurnal) tidally induced currents, which are typically in the order of 1 – 1.5 m/s (Wang et al., 2002). The river discharge ranges between 50 and 200 m^3/s (van Rijn, 2011), meaning that approximately $\sim 10^6$ m^3 of fresh water enters the estuary per semidiurnal tidal cycle. Given the fact that this discharge is less than 1% of the tidal prism ($\sim 10^9$ m^3 per semidiurnal tidal cycle), the estuary is regarded as well-mixed with negligible fluvial sediment input. Measurements of the free surface elevation along the estuary show that the mean tidal range (difference between high and low water, averaged over one neap-spring tidal cycle) increases from about 3.8 m at the mouth to 5.2 m near Rupelmunde (~89 km from the mouth), after which it decreases farther landward. The bed of the Western Scheldt Estuary consists of mainly medium to fine sand, with a grain size diameter d_{50} of 200 μm on average, and with less than 10% mud in the channels and on the shoals (Wang et al., 2002). The grain size diameter in the channels is generally larger than that on the shoals.

3. Material and Methods

3.1. Model Description

In this study, the Delft3D hydrodynamic and morphodynamic model is used in two-dimensional (depth-averaged) mode. An idealized modeling approach is applied by schematizing the tidal forcing and initial bathymetry and excluding as many processes as possible (such as waves, wind, and sea level rise). Below, an overview of the equations that govern hydrodynamics, sediment transport, and bed level update is presented. Further details are given in Lesser et al. (2004) and the Delft3D user manual (Deltares, 2016).

The hydrodynamics considered are described by full nonlinear shallow water equations

$$\frac{\partial D}{\partial t} + \frac{\partial (Du)}{\partial x} + \frac{\partial (Dv)}{\partial y} = 0, \tag{1}$$

$$\frac{\partial u}{\partial t} + u\frac{\partial u}{\partial x} + v\frac{\partial u}{\partial y} - fv = -g\frac{\partial \eta}{\partial x} - \frac{g\sqrt{u^2+v^2}}{C^2 D}u + \frac{1}{D}\left[\frac{\partial}{\partial x}\left(D\nu\frac{\partial u}{\partial x}\right) + \frac{\partial}{\partial y}\left(D\nu\frac{\partial u}{\partial y}\right)\right], \tag{2}$$

$$\frac{\partial v}{\partial t} + u\frac{\partial v}{\partial x} + v\frac{\partial v}{\partial y} + fu = -g\frac{\partial \eta}{\partial y} - \frac{g\sqrt{u^2+v^2}}{C^2 D}v + \frac{1}{D}\left[\frac{\partial}{\partial x}\left(D\nu\frac{\partial v}{\partial x}\right) + \frac{\partial}{\partial y}\left(D\nu\frac{\partial v}{\partial y}\right)\right]. \tag{3}$$

Here, D is the local water depth, u and v are the depth-averaged velocities in the eastern (x) and northern (y) directions, respectively (Figure 2a), f is the Coriolis parameter, g is the acceleration due to gravity, η is the sea surface elevation with respect to the undisturbed water level (= MSL), C is the Chézy coefficient, ν is the horizontal eddy viscosity, here assumed to be spatially uniform, and t is time. Because of the meandering geometric shape of the estuary under consideration, effects of curvature on hydrodynamics are accounted for by including secondary flow (Kalkwijk & De Vriend, 1980).

The sediment transport formula applied in this model is Engelund and Hansen (1967). This formula estimates the total transport vector $\vec{q}_0$ (sum of bed load transport and suspended load transport), which is in the direction of $\vec{v}$, according to

$$\vec{q} = \frac{0.05\alpha|\vec{v}|^4}{\sqrt{g}C^3\delta^2 d_{50}}\vec{v}, \tag{4}$$

where α is a calibration coefficient (order 1); $|\vec{v}| = \sqrt{u^2+v^2}$ is the magnitude of flow velocity; $\delta = (\rho_s - \rho_w)/\rho_w$ is the relative density with ρ_s and ρ_w the sediment and water densities, respectively; and d_{50} is the median grain size. Bed slope effects are accounted for in both the direction of the local flow (longitudinal bed slope) and in the direction perpendicular to that (transverse bed slope), with bed slope coefficients α_{BS} and α_{BN}, respectively. For a detailed description see the Delft3D user manual (Deltares, 2016).

The bed level change is determined by computing the divergence of sediment transport vector $\vec{q}$ (with components q_x and q_y) or

$$\frac{\partial z_b}{\partial t} = -\frac{1}{1-p}\left[\frac{\partial q_x}{\partial x} + \frac{\partial q_y}{\partial y}\right], \tag{5}$$

with p the porosity of the bottom layer (equal to 0.4). The morphodynamic timescale is much longer (order years to decades) than the hydrodynamic timescale (order days), which allows for accelerated bed level change by multiplying the time in the above equation by a factor α_{MOR} (Latteux, 1995; Roelvink, 2006; Zeinali et al., 2014).

At offshore boundaries, a combination of water level boundary conditions ζ at the western boundary and Neumann boundary conditions at the southwestern and northeastern boundaries is applied (Figure 2), as proposed by Roelvink and Walstra (2004). Specifically, at the western boundary the model is forced by a tidal wave with three harmonic constituents (M_2, M_4, and M_6) with amplitudes $\hat{\zeta}_2$, $\hat{\zeta}_4$, and $\hat{\zeta}_6$; angular frequencies ω, 2ω, and 3ω; and phases ϕ_2, ϕ_4, and ϕ_6, which travels from southwestern to northeastern boundaries. Note that other harmonic constituents (such as S_2) are excluded from the tidal forcing, as their contributions to the long-term mean sediment transport is small (Van de Kreeke & Robaczewska, 1993). At the offshore boundaries, an equilibrium sediment transport is set, which means that sediment transport entering or exiting through the boundaries is determined by local flow conditions and very little accretion or erosion is experienced near these boundaries (Deltares, 2016). At the landward boundary, near Ghent, the along-channel transport of fluid and sediment is set to zero.

3.2. Methodology

3.2.1. General Setting

The model solves the equations on a curvilinear, staggered grid, as depicted in Figure 2a (red lines). The grid covers the entire Scheldt Estuary and part of the North Sea, thereby extending from Ghent to ~30 km seaward. The size of grid cells ranges between 100 m and 300 m in the area of interest (Western Scheldt), and it increases to ~2.5 km at the offshore boundaries. Values of the amplitudes and phases of the three harmonic constituents (M_2, M_4, and M_6) imposed at the offshore boundaries are determined from a spatial interpolation between closest stations where tidal amplitudes and phases are measured (see Table 1). Based on observed sediment characteristics in the Western Scheldt (section 2.3), noncohesive sediment is assumed with a single size of $d_{50} = 200$ μm. An erodible layer with a uniform thickness of 50 m is used in the model. Nonerodible side walls are considered, consistent with the fixed lateral boundaries of the estuary. The morphological acceleration factor α_{MOR} is 100, which is often used in morphodynamic studies of tidal embayments (cf. Canestrelli et al., 2013; Chu et al., 2011; Van der Wegen & Roelvink, 2012). With a hydrodynamic time step Δt of 15 s, the morphodynamic time step is thus 25 min. Test runs with other values of α_{MOR} (ranging from 25 to 400) show that results are not significantly different. A more detailed discussion of the methodology can be found

Table 1
Overview Model Parameters

	Parameter	Value	Description
Flow	f	1.43×10^{-4} s^{-1}	Coriolis parameter
	C	65 m$^{1/2}$s^{-1}	Chézy coefficient
	ν	1 m^{2}s^{-1}	Eddy viscosity
	$(\hat{\zeta}_{2,S};\phi_{2,S})$ / $(\hat{\zeta}_{2,N};\phi_{2,N})$	(1.6 m; 23°/(1.2 m; 55°),	(Amp.;Phase) M_2 South (S)/North (N)
	$(\hat{\zeta}_{4,S};\phi_{4,S})$ / $(\hat{\zeta}_{4,N};\phi_{4,N})$	(0.1 m; −11°)/(0.1 m; 113°),	(Amp.;Phase) M_4 South (S)/North (N)
	$(\hat{\zeta}_{6,S};\phi_{6,S})$ / $(\hat{\zeta}_{6,N};\phi_{6,N})$	(0.05 m; −24°/(0.05 m; 77°),	(Amp.;Phase) M_6 South (S)/North (N)
	ω	1.405×10^{-4}s^{-1}	Angular frequency M_2 tide
Sediment	α	1	Calibration coefficient
	δ	1.65	Relative density of sediment
	d_{50}	0.2 mm	Diameter grain size
	α_{BS}	1	Longitudinal bed slope coefficient
	α_{BN}	2	Transverse bed slope coefficient
	p	0.4	Porosity bed
Numerics	Δt	15 s	Time step
	α_{MOR}	100	Morphological amplification factor
	Δx, Δy	100–300 m	Range of size grid cells in the study area

Note. Water level data provided by Rijkswaterstaat (Ministry of Infrastructure and the Environment, The Netherlands) are used to derive amplitudes and phases of the different tidal constituents imposed at offshore boundaries.

in the supporting information (Dam et al., 2016; Eelkema, 2013; Fletcher & Spencer, 2005; Kuijper et al., 2004; Madsen et al., 2007; Morris et al., 2002; Van Rijn, 2007; Wahl et al., 2013; Van der Wegen & Roelvink, 2012; Zitman, 1999). An overview of all model parameters is presented in Table 1.

Model experiments start from an idealized bathymetry (Figure 5a), which is based on the piecewise linear fit to the width-averaged bed level $\langle z_b \rangle$ shown in Figure 3b (red line). The total simulation time period is chosen such that within this time, bed level development is relatively small compared with its initial development. Quantitatively, a global growth rate σ (year^{-1}) of bottom patterns is defined, following Garnier et al. (2006) and Nnafie et al. (2014), as

$$\sigma \equiv \frac{\iint_{A_{\mathrm{WS}}} h \frac{\partial h}{\partial t} \mathrm{d}x\mathrm{d}y}{\iint_{A_{\mathrm{WS}}} h^2 \mathrm{d}x\mathrm{d}y}, \tag{6}$$

with h the bed level change given by $h = z_b(x, y, t) - z_b(x, y, t = 0)$, and A_{WS} is the horizontal surface area of the Western Scheldt (m^2) at high water. The total simulation time period is chosen such that within this time, growth rate σ decreases to less than 1% of its initial value σ_0, with the latter defined as the average value over the first 5 years. As preliminary model simulations show that a simulation period of 300 years is sufficient to fulfill the latter condition, most of simulations are run for this time period. Each simulation lasts about 8 days using a 12 Core Intel Xeon Westmere X5650 - 2.66 GHz. However, to ensure that model results do not depend on the default simulation time (300 years), some simulations are conducted for longer time periods (600 years).

3.2.2. Overview Model Experiments

Analysis of most of the experiments carried out in the present study focuses on the spatial differences between channel network configurations obtained in cases with and without the presence of a secondary basin. To this end, an experiment is performed (run "Reference" in Table 2) without the presence of a secondary basin, whereby the present-day geometric shape of Scheldt Estuary is used (Figure 5a).

To achieve the first objective, a run is performed in the presence of a single secondary basin (hereafter, abbreviated as SB), which is placed perpendicular to the estuary axis at approximately the same location (~7 km from the mouth) as that of former secondary basin Sloe (experiment "SBN1" in Table 2). The dimension used for the SB are derived from those of former secondary basin Sloe (Figure 2b), but its shape is simplified such

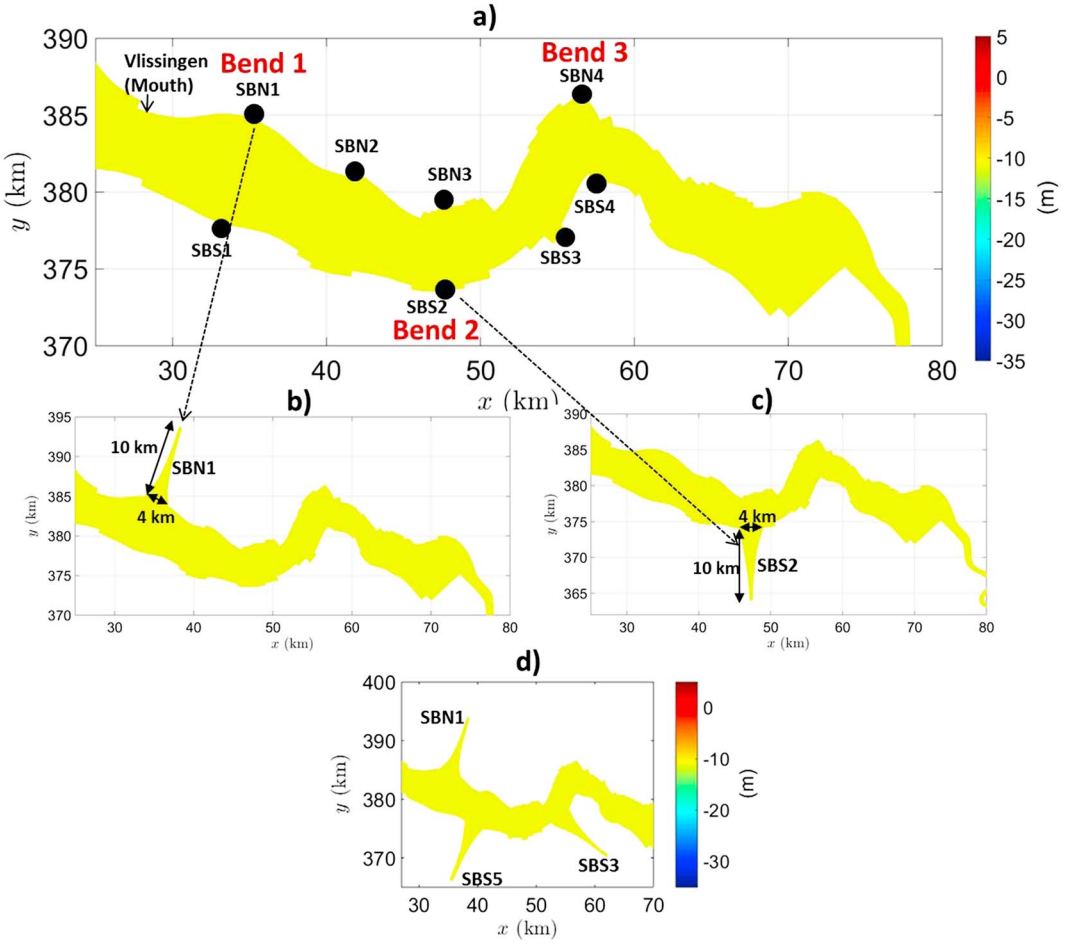

Figure 5. (a) Locations of secondary basins (SB) within the estuary (black dots). Colors indicate the initial bed level z_b ($t = 0$) in this area. Letters "N" and "S" refer to northern and southern banks of the estuary. Examples of schematized secondary basins: (b) basin SBN1 and (c) basin SBS2. Bend 1, Bend 2, and Bend 3 indicate the seaward, middle, and landward bends of the estuary, respectively. (d) Geometric shape of the estuary in case that three secondary basins are placed at approximately the same locations of former basins Sloe, Braakman, and Hellegat (Figure 2b).

that it represents a basin with an exponentially decreasing width (w_b). The latter is 4 km at the transition to the estuary (Figures 5b and 5c), and it decreases over a length scale l_b, which is chosen such that the horizontal surface area of the SB approximately equals the total Sloe area reclaimed between 1800 and 1970 ($\sim 1.3 \cdot 10^7$ m^2, Zitman (1999); $l_b = 10$ km). The width of the SB at its landward end is about 0.5 km.

To investigate the sensitivity of model results to location, number, and geometry of secondary basins (second objective), first, a series of model runs are conducted by placing the single basin at distances 7, 14, 21, 28, and 35 km from the mouth near Vlissingen, thereby covering the entire meandering length of the estuary (~28 km), which extends from the seaward bend (Bend 1 in Figure 5a) to the landward bend (Bend 3). Because of the curved geometric shape of the estuary, both inner and outer bends are considered. Specifically, basins SBNi and SBSj are placed at the northern and southern banks of the estuary, respectively, with $i = 2, 3, 4$ and $j = 1, 2, 3, 4$ (run series "Single"). Exact locations of these basins are shown in Figure 5a (black dots). Next, a series of runs are performed to examine sensitivity of model results to the numbers of SBs by adding two and three secondary basins to the estuary (run series "Double" and "Triple"). In run "Double", all possible combinations of basin SBN1 with other basins are considered, while in run "Triple", the basins have approximately the same locations as those of Sloe, Braakman, and Hellegat (Figure 5d). Finally, to examine the dependence of model results on the used geometry of the SB, four additional experiments are carried out (series "Geometry" in Table 2). In the first experiment, the length of SBN1 is halved ($l_b = 5$km, run "SBN1-Short"), and in the second, the SBN1 is twice as long ($l_b = 20$km, run "SBN1-Long"). In the third experiment, the width of SBN1 is halved ($w_b = 2$ km, run "SBN1-Narrow"), and in the fourth, SBN1 is twice as wide ($w_b = 8$ km, run "SBN1-Wide").

Table 2
List of Model Runs

Name runs	Description
Reference	Present geometry, no SB
SBN1	1 SB; located at ~7 km from the mouth
Single	1 SB: either north (SBNi, $i = 2, 3, 4$) or south (SBSj, $j = 1, 2, 3, 4$)
Double	2 SB: SBN1 + SBNi, $i = 2, 3, 4$; SBN1 + SBSj, $j = 1, 2, 3, 4$
Triple	3 SB: SBN1 + SBS5 + SBS3
Geometry	SBN1-Short, SBN1-Long, SBN1-Wide, SBN1-Narrow
SBN1 ON/OFF	$t \leq 300$ years: with SBN1;
	$t > 300$ years: SBN1 removed
SBN1 ON/OFF stepwise	$t \leq 300$ years: with SBN1;
	$300 < t \leq 400$ years: half of SBN1 area removed (landward part)
	$t > 400$ years: other half removed
SBN1-SBS5-SBS3 ON/OFF	$t \leq 300$ years: with SBN1, SBS5, and SBS3;
	$t > 300$ years: all secondary basins are removed

Note. Here SBNi and SBSj mean that a secondary basin (SB) is located at northern and southern banks of the estuary, respectively, at location with indices i and j within the estuary. Indices $i = [1, 2, 3, 4]$ and $j = [1, 2, 3, 4]$ stand for locations $[7, 14, 21, 35]$ km and $[7, 21, 28, 35]$ km, respectively, with respect to the mouth of the estuary.

To test the hypothesis that the removal of an SB will result in channel displacement toward the bank of the estuary where the basin was located, three more experiments are performed to mimic the closure of former basins Sloe, Braakman, and Hellegat (third objective). In the first experiment (run "SBN1 ON/OFF"), between $t = 0$ and $t = 300$ years, the model is run in the presence of one single basin (SBN1), after which this basin is removed in the subsequent time period. The same methodology is employed in the second experiment (run "SBN1-SBS5-SBS3 ON/OFF"), with the difference that now three basins are placed at approximately the same locations of Sloe, Braakman, and Hellegat (Figure 5d), which are removed at $t = 300$ years. Finally, to quantify the effects of a gradual closure of the basin on model results, a third experiment is carried out (run "SBN1 ON/OFF stepwise"), where half of SBN1 basin area (landward part) is removed at $t = 300$ years, and the remaining part at $t = 400$ years. These final three experiments have a simulation time of 600 years.

4. Results

4.1. Single Secondary Basin

Figure 6 shows snapshots of bed level development after 150 and 300 years of morphodynamic evolution in cases without (a–c) and with a secondary basin (SBN1, d–f). The obtained channel network configurations at $t = 300$ years are depicted in Figure 6g. These network configurations hardly change after $t = 300$ years, although bed level changes still take place on longer timescales. Note that in spite of the fact that growth rate σ defined in equation (6) keeps on decreasing after $t = 300$ years, a morphodynamic equilibrium state with vanishing σ is not reached within the maximum simulation time period considered in this study (600 years). From Figure 6g it appears that significant spatial differences exist between channel configurations of cases with (red color) and without SBN1 (gray color). In the former case, channels $c3$ and $c6$ are much narrower, channel $c1$ ($c8$) is less (more) pronounced compared with those that form in the latter case. Moreover, the channel that forms in the vicinity of SBN1 ($c0$) is located farther away from the bank of the estuary with respect to its position in the case without this basin. Eventually, this difference in channel location between the two cases (hereafter referred to as "channel location difference Δ") is $\Delta \sim 0.8$ km (Figure 6h).

4.2. Location and Number of Secondary Basins

Results from sensitivity experiments to the location of the SB (experiment series "Single" in Table 2) are presented in Figure 7. Overall, channel $c5$ does not form for most locations of the SB. In the case of SBN2 (Figure 7b), both channels $c2$ and $c5$ do not appear, implying that northern and southern channels are disconnected from each other. By plotting channel location difference Δ as a function of the location of the SB with respect to the mouth of the estuary (Figure 7i), it appears that for most cases with SB (SBN1, Figure 7a; SBN2, Figure 7b; SBN3, Figure 7c; SBN4, Figure 7d; SBS1, Figure 7e; SBS2, Figure 7f) the presence of the basin

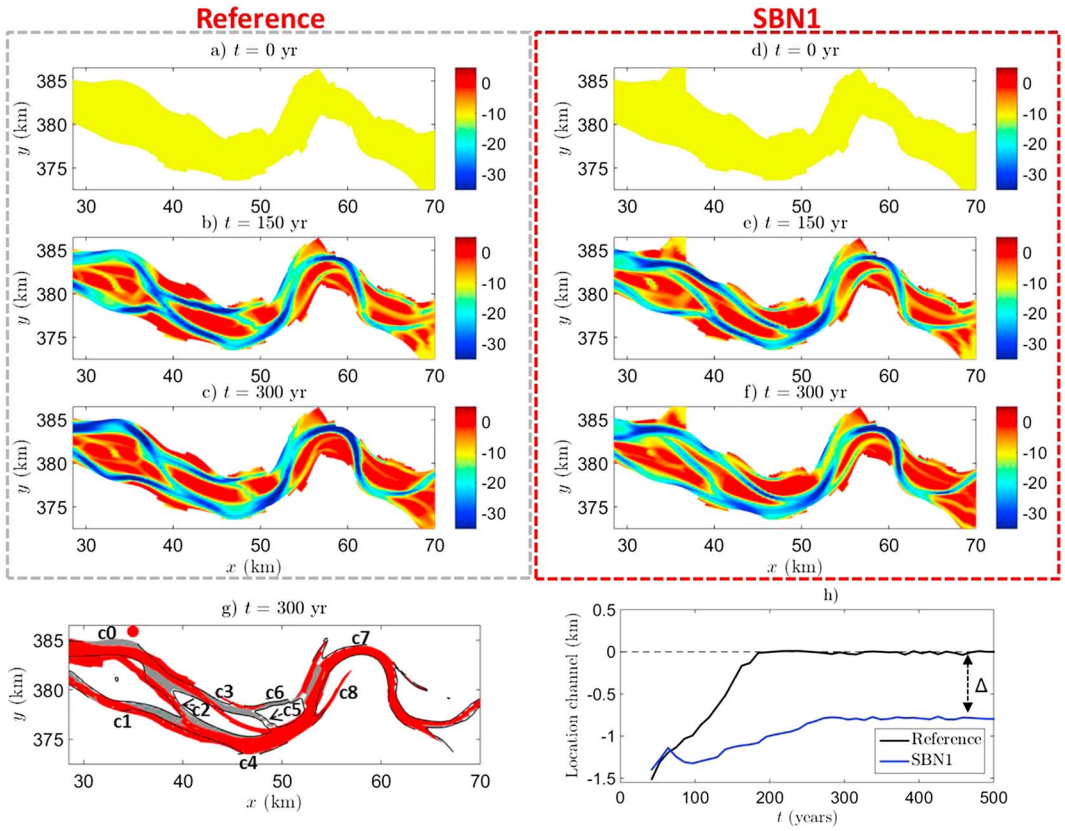

Figure 6. (a–f) Snapshots of bed level development between $t = 0$ and $t = 300$ years in the cases without and with SB (runs "Reference" and SBN1 in Table 2, respectively). (g) Channel network configurations at $t = 300$ years in the reference case (gray color) and in the case of SBN1 (red color), which are extracted from the bed level distribution in Figures 6c and 6f. Only channels with $z_b < -10$m are included in these networks. Notations $c0$, $c1$, ..., $c8$ denote the different branches of the network in the reference case. (h) Time evolution of the location of channel near SBN1 in cases without (black line) and with SBN1 (blue line). Here channel location is defined with respect to the final position of the channel in case without SB. The arrow denotes difference in the final channel location between cases with and without SBN1 (referred to as channel location difference Δ).

causes the nearby channel to form farther away from the bank of the estuary with respect to its position in the case without this basin. Note that the large value of Δ in cases of basins SBN3 and SBN4 is due to the fact that in these cases the main channel ($c8$) forms along the southern bank in the area of the strong estuary bend (Figures 7c and 7d). In the cases of basins SBS3 and SBS4, channel location difference is not clear (not plotted in Figure 7i), probably due to the fact that channel $c7$ is too far away for these basins to induce a channel location difference. In contrast, the presence of the latter basins rather seems to enhance the formation of two channels in the area of the strong estuary bend (Figures 7g and 7h). Formation of a two-channel system in the latter area occurs also in cases of SBN2 and SBS2 (Figures 7b and 7f), and to a lesser extent in case of SBN1 (Figure 7a). The large spatial differences between channel network configurations that form in cases with and without SB in this area compared with those elsewhere in the estuary is likely related with the strong curved shape of the estuary in this region, suggesting that constructing a SB in areas where the estuary strongly curves will induce significant spatial changes in the channel network configuration in these areas. Finally, Figure 7i further reveals that no fundamental differences exist between results in cases that a SB is located at the inner and outer bends, although this figure suggests that channel location difference is generally larger in the former case.

Regarding the effects of the number of secondary basins on the channel network configurations, Figure S1 in the supporting information shows that results in case with two secondary basins are not fundamentally different from those in case with one single basin. Similarly, the difference in channel location appears in the vicinity of the individual basins (Figures S1a–S1f), suggesting that the total response of the channel network to the presence of two secondary basins is a linear superposition of its separate response to each of the basins.

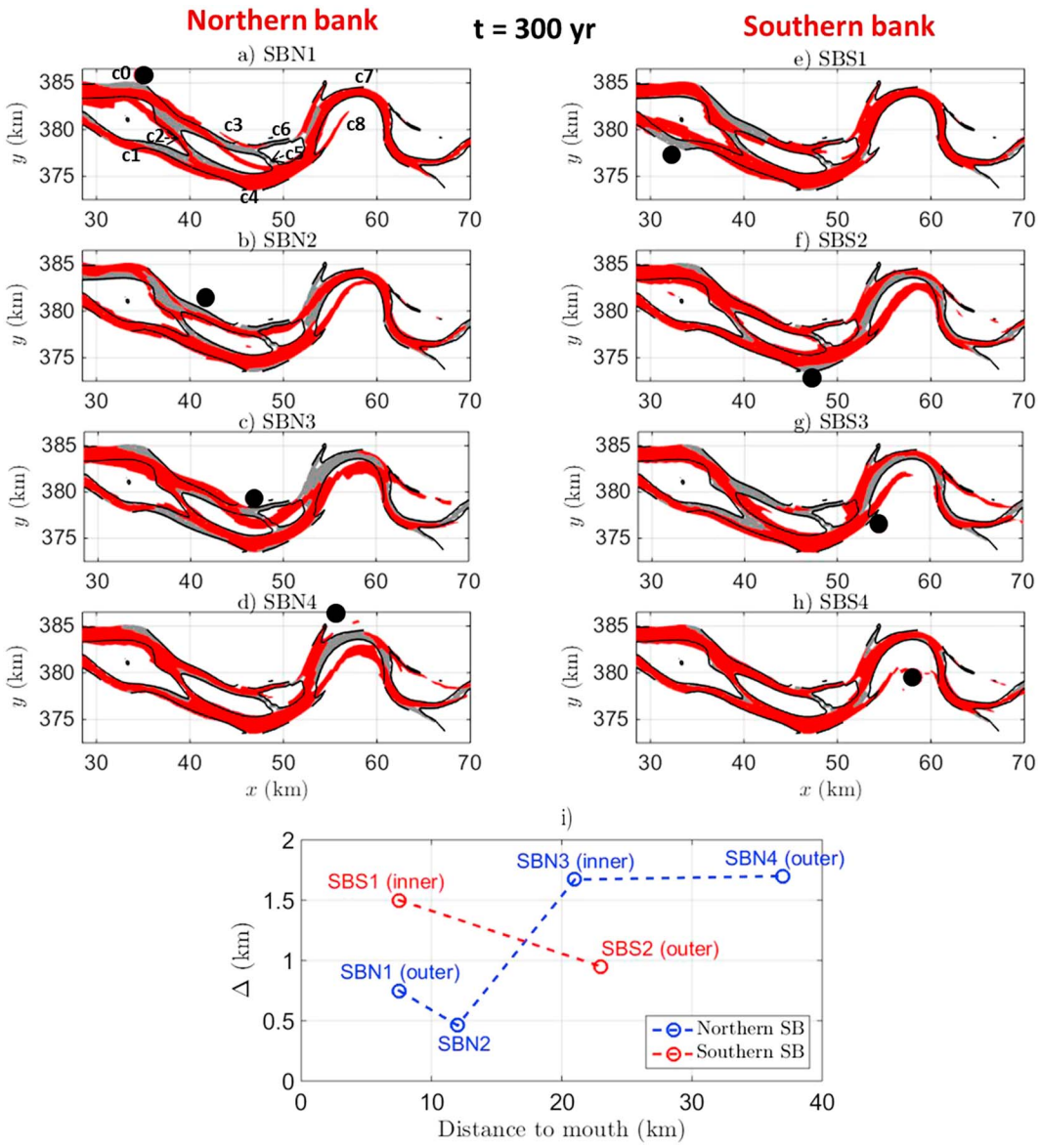

Figure 7. Obtained channel network configurations after 300 years (red color) in cases of different locations of the SB along the estuary. Results in cases of (a–d) northern and (e–h) southern located SBs. Locations of the SBs are denoted by black dots. Channel network configuration obtained in the reference case is also shown (gray color). Notations *c*0, *c*1, ..., *c*8 in Figure 7a denote the different branches of the network. (i) Channel location difference Δ as a function of the distance of the SB to the mouth of the estuary. The "inner" and "outer" between parentheses indicate that the SB is located at inner and outer bends, respectively. Channel location is determined based on its maximum depth. Differences Δ for cases of basins SBS3 and SBS4 are not clear, and therefore, they are not plotted.

However, this superposition principle does not seem to apply in the case that three secondary basins are present (Figure S1i). This is because in the latter case the channel near SBS5 is located closer to this basin, with respect to the reference case, whereas in the presence of one-single SB at this location the nearby channel is located farther away (result not shown). Furthermore, also in the cases of two and three SBs, the formation of a two-channel (single channel) network is enhanced if a SB is located close to the outer (inner) bend of the estuary.

4.2.1. Basin Geometry

Results from sensitivity experiments to the geometry of SB (run series Geometry) are shown in Figure 8a, which displays channel location difference Δ as a function of length *l*, width *w*, and surface area *A* of the SB. The corresponding channel network configurations are depicted in Figure S2 of supporting information. Clearly, also in cases of different geometries of the SB, channel location differences occur. However, from Figure 8a

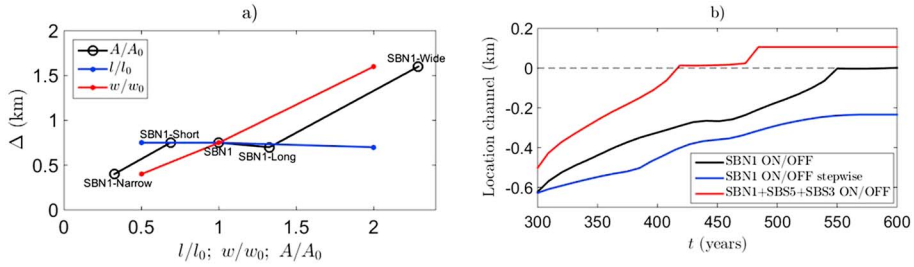

Figure 8. (a) Channel location difference Δ for different lengths *l* (blue line) and widths *w* (red line) of the SB. Black line represents difference Δ as a function of the surface area of the SB. Length *l*, width *w*, and surface area *A* are scaled by their corresponding values in case of the default geometry, l_0 (= 10 km), w_0 (= 4 km), and A_0 (= $13 \cdot 10^6$ m^2), respectively. (b) Channel location in the vicinity of SBN1 as a function of time in cases of run series SBN1 ON/OFF (black line), SBN1 ON/OFF stepwise (blue line), and SBN1+SBS5+SBS3 ON/OFF (red line). Channel location is computed with respect to its final position in case of run SBN1 ON/OFF (black line).

it is seen that difference Δ strongly depends on the width of the basin. The larger the width, the farther away the nearby channel forms. Note the fact that a larger surface area *A* resulting from increasing the length of SB (SBN1-Short, SBN1, and SBN1-Long; Figure 8a) does not cause a larger difference Δ. This demonstrates that the width of the SB fully governs the location of the channel near this basin. Figure S2 of supporting information further shows that a two-channel network forms in the strong estuary bend in some cases with SB, which again reveals the large sensitivity of the channel network in areas where the estuary strongly curves to the presence of a SB.

4.2.2. Removing Secondary Basins

Results on effects of removing a secondary basin on the long-term evolution of the nearby channels are presented in Figure 8b, which compares the time evolution of the location of the channel near SBN1 between cases SBN1 ON/OFF (black line), SBN1+SBS5+SBS3 ON/OFF (red line), and SBN1 ON/OFF stepwise (blue line). Snapshots of the corresponding channel network configurations are shown in Figure S3 of supporting information. Figure 8b demonstrates that channels, which are located in the vicinity of a secondary basin, migrate toward the bank of the estuary after removing the SB. In the case of SBN1 ON/OFF and SBN1+SBS5+SBS3 ON/OFF, a total displacement of ~0.6 km is covered by the nearby channel after removal of SBN1, while the displacement in case of stepwisely removing SBN1 is smaller (~0.4 km). In the case of SBN1+SBS5+SBS3 ON/OFF, channel displacement near basins SBS5 and SBS3 is smaller (~0.3 km) than that near SBN1 (~0.6 km).

Furthermore, from Figure 8b it appears that channel displacement in the cases of SBN1 ON/OFF and SBN1 ON/OFF stepwise lasts longer (~250 years) than that in case of SBN1-SBS5-SBS3 ON/OFF (~180 years).

5. Discussion

5.1. Physical Mechanisms

By comparing the spatial distribution of the net sediment transport $\overline{\vec{q}}$ (with the overbar denoting averaging over M_2-tidal period *T*) between cases without and with SB at the start of the model simulation ($t = 0$), it turns out that convergence of sediment occurs at the entrance of the SB (Figure 9b). Consequently, a shoal develops over time at this location (Figure 9d), which "pushes" the channel to form farther away from the bank of the estuary (Figure 9f) compared with the case without SB (Figure 9e).

To obtain insight into the mechanisms causing sediment convergence at the entrance of the SB, the relative contributions associated with residual velocity and tidal asymmetry to the net sediment transport are analyzed. First, the *x*-*y* components of the tidal velocity vector $\vec{v}$ (= u, v) are decomposed into contributions related to tidal constituents M_0, M_2, and M_4, as follows:

$$u = u_0 + \hat{u}_2 \cos(\omega t - \phi_2) + \hat{u}_4 \cos(2\omega t - \phi_4), \tag{7}$$

$$v = v_0 + \hat{v}_2 \cos(\omega t - \psi_2) + \hat{v}_4 \cos(2\omega t - \psi_4), \tag{8}$$

in which components (u_0, v_0) are Eulerian residual velocities, respectively; $(\hat{u}_2, \hat{v}_2)$ and $(\hat{u}_4, \hat{v}_4)$ are, respectively, the amplitudes of M_2 and M_4 tidal velocities; (ϕ_2, ψ_2) and (ϕ_4, ψ_4) are their corresponding phases; and ω is the M_2 angular frequency. Note that for simplicity, the contribution associated with M_6 is excluded from this analysis, as it is small compared to those associated with M_2 and M_4.

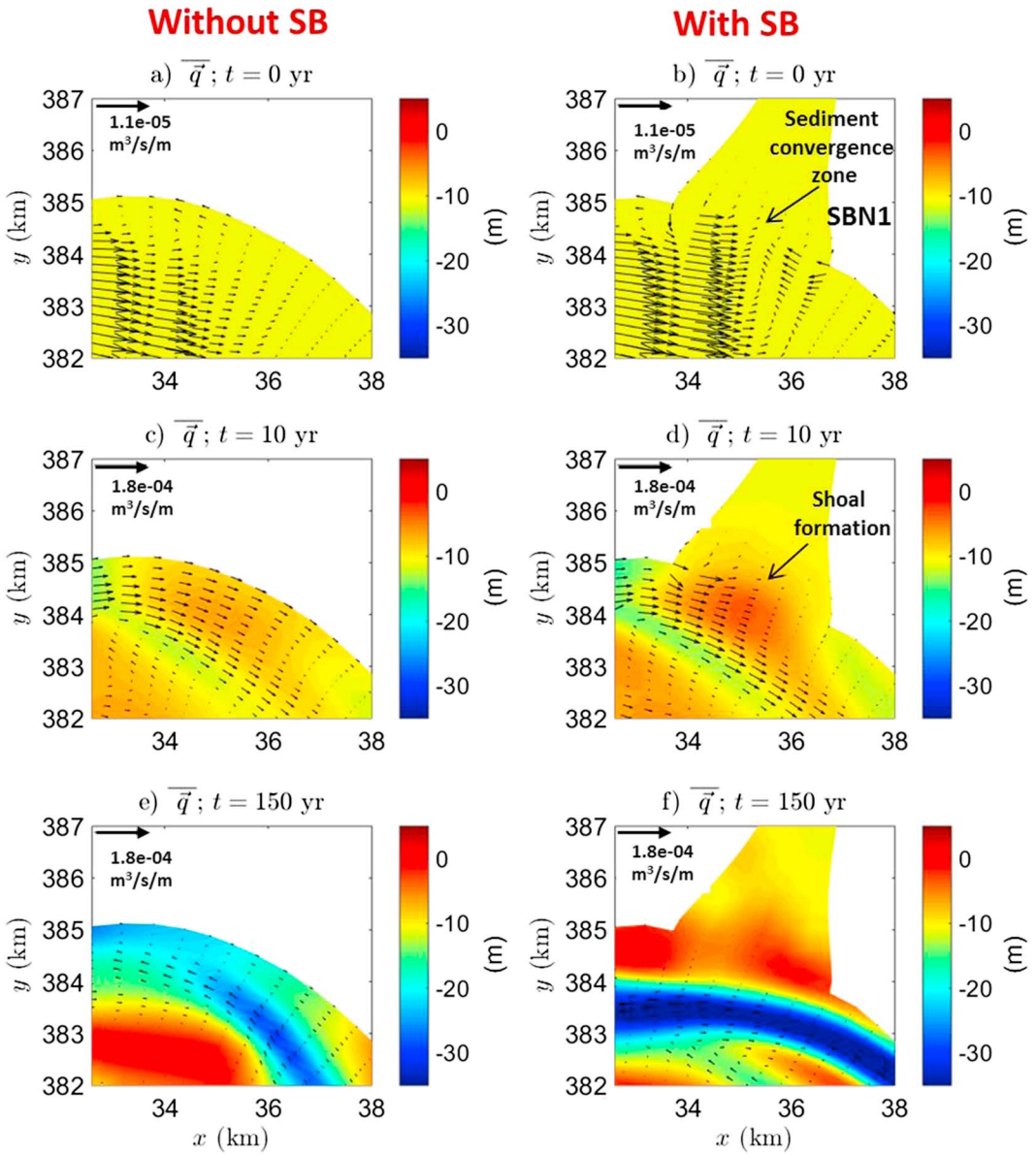

Figure 9. Bed level z_b (colors) and tidally averaged sediment $\overline{\vec{q}}$ (arrows; overbar indicates averaging over M_2-tidal period) in the x-y domain at times (a and b) $t = 0$, (c and d) $t = 10$ years, and (e and f) $t = 150$ years in the cases without (Figure 9a, 9c, and 9e) and with (Figures 9b, 9d, and 9f) SB.

Next, to find approximate expressions for the net sediment transport in x and y directions ($\overline{q}_x, \overline{q}_y$), it is assumed that $u_0, v_0 << \hat{u}_2, \hat{v}_2$; and $\hat{u}_4, \hat{v}_4 << \hat{u}_2, \hat{v}_2$. If only the first-order terms are taken (terms linear in $u_0, v_0, \hat{u}_4, \hat{v}_4$), components $\overline{q}_x$ and $\overline{q}_y$ are approximated by

$$\overline{q}_x = \frac{\mathcal{F}}{T}\int_0^T (u^2+v^2)^2 u dt \approx \mathcal{F}\left(T_{1x}+T_{2x}\right), \qquad \mathcal{F} = \frac{0.05\alpha}{\sqrt{g}C^3\delta^2 d_{50}}, \tag{9}$$

$$\overline{q}_y = \frac{\mathcal{F}}{T}\int_0^T (u^2+v^2)^2 v dt \approx \mathcal{F}\left(T_{1y}+T_{2y}\right). \tag{10}$$

Components T_{1x}, T_{1y} ($= \vec{T}_1$; exact expressions are given in equation (A1)) describe the net sediment transport related with residual flow $\vec{v}_o$ ($= u_o, v_o$) and tidal eccentricity. The latter is associated with the phase difference between velocity components u and v ($\phi_2 - \psi_2$). Circular tides ($\phi_2 - \psi_2 = 90°$) result in smaller residual

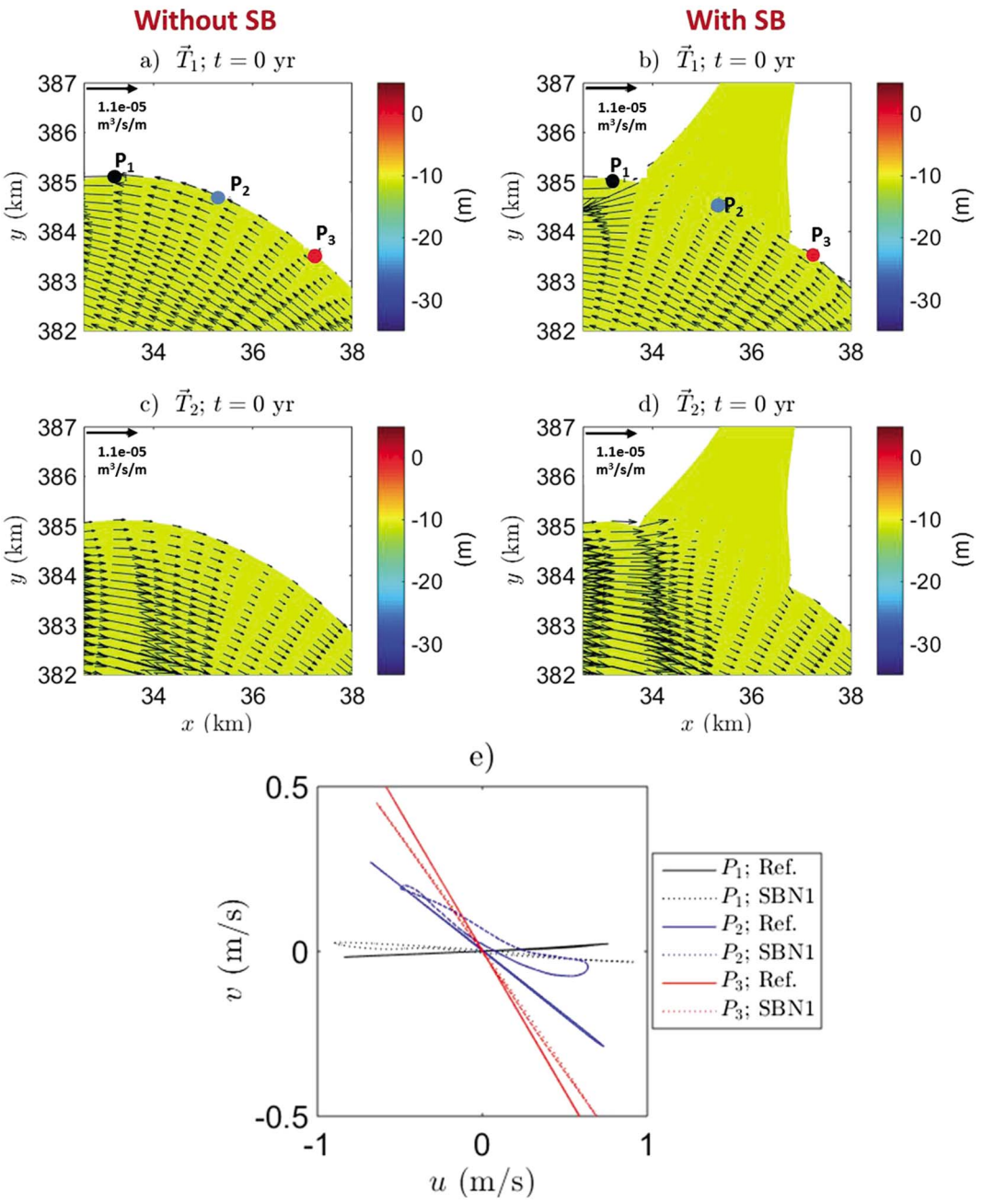

Figure 10. Bed level z_b (colors) and relative contribution to net sediment transport (arrows) by terms (a and b) T_1 and (c and d) T_2 in the x-y domain at time $t = 0$ in cases without (Figures 10a and 10c) and with (Figures 10b and 10d) a SB (SBN1). (e) Plots of tidal ellipses (v versus u over one tidal cycle) at locations P_1 (black), P_2 (blue), and P_3 (red) (indicated in Figures 10a and 10b) in case without (solid lines) and with (dotted lines) SB.

sediment transport compared with bidirectional tides ($\phi_2 - \psi_2 = 0°$). Both residual flow $\vec{v}_o$ and phase difference $\phi_2 - \psi_2$ determine the direction and magnitude of the net sediment transport $\vec{T}_1$. Positive (negative) values of transport vector $\vec{T}_1$ means that the latter is flood (ebb) directed. Net sediment transport due to tidal asymmetry is described by components T_{2x}, T_{2y} (= $\vec{T}_2$) in equation (A2). Phase difference between M_2 and M_4 tidal currents as well as eccentricity controls the magnitude and direction of $\vec{T}_2$.

The spatial distribution of contributions $\vec{T}_1$ and $\vec{T}_2$ in cases with and without SB at the start of the simulation ($t = 0$) is compared in Figure 10. The latter figure reveals that the presence of the SB along the estuary decreases the magnitude of contributions $\vec{T}_1$ and $\vec{T}_2$ (Figures 10b and 10d), such that sediment is deposited

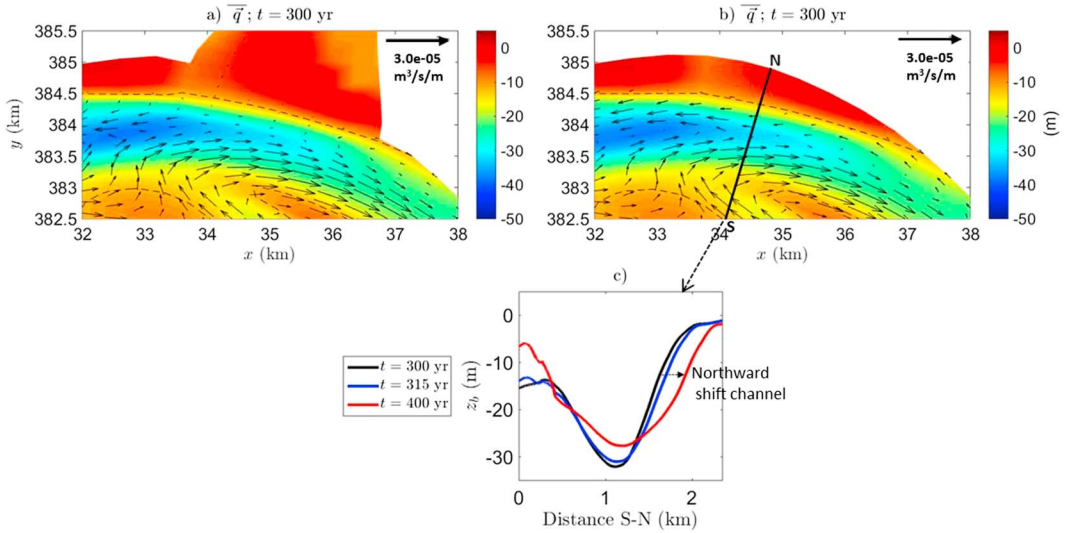

Figure 11. (a and b) Bed level z_b (colors) with superimposed net sediment transport $\overline{\vec{q}}$ in the area of the SB (SBN1) before and after removing the basin at t = 300 years. Dashed line denotes the −10 m contour level. (c) Time evolution of bed level profile along the cross-channel transect depicted in Figure 11b (black solid) in the first 50 years after removing the SB.

in the vicinity of the SB, resulting in shoal formation over time. Figure 10e demonstrates that the weakening of the ebb-directed transport $\vec{T}_1$ in front of the SB is caused by a reduction of tidal velocity as well as an increase of the phase difference $\phi_2 - \psi_2$ between components u and v in this region (blue dotted line). Further analysis reveals that weakening of magnitude of $\vec{T}_2$ near the SB is caused mainly by changes in terms associated with the phase difference between M_2 and M_4 tidal velocities (first term on the right-hand side of equation (A2). Eccentricity effects on magnitude of $\vec{T}_2$ are less dominant.

From Figure 9b (and also from Figure 10) it is further seen that formation of a sediment convergence zone near the SB is mostly due to changes in the sediment transport field inside the estuary rather than due to a sediment exchange between the estuary and the SB. The latter might explain the fact that channel location difference is particularly determined by the width of the basin, rather than its length. This is because a wider SB causes enhanced sediment convergence, resulting in the formation of a larger shoal area near the basin, compared with a narrower SB.

Finally, with regard to the effects of removing a SB on location of the nearby channel, it appears that erosion is enhanced at the northern margin of this channel, immediately after the removal. This is shown in Figures 11a and 11b, which compares the net sediment transport before and after removing SBN1. Apparently, removing the basin causes stronger and more bidirectional (weaker eccentricity) tidal currents north of the nearby channel, resulting in enhanced erosion in this area. Consequently, the channel starts to migrate northward, thereby eroding the shoal that formed prior to removing the SB (Figure 11c).

5.2. Comparison With Observations

5.2.1. Western Scheldt Estuary

Model results demonstrate that channels that are located near a SB migrate toward the bank of the estuary after removing the basin. Modeled timescales of channel displacement (order decades to centuries) seem to be consistent with observations, particularly in the case of removing three basins. These outcomes provide support for the hypothesis that closure of secondary basins Sloe, Braakman, and Hellegat in the Western Scheldt Estuary is responsible for the observed lateral shift of the nearby channels. A significant difference between model results and observations is that the computed lateral displacements of the channel near basins SBN1, SBS5, and SBS3 are smaller than the observed displacements near Sloe, Braakman, and Hellegat. By comparing the observed channel network configuration in 1800 (before closure of Sloe) with the modeled configuration in the case of SBN1 (Figure S4 in supporting information), it appears the channel near Sloe was located more southward (gray color) compared with the location of the channel near SBN1 obtained from the model (red color). This means that after the (gradual) closure of Sloe, the nearby channel could shift over

a larger distance toward the northern bank of the estuary compared with the channel near SBN1, explaining the larger displacement of the channel in the observations compared with model results. The difference in channel location between observations and model results is attributed to the fact that the shoal area that was located near Sloe in 1800 (Figure 3a, top left) was larger and was extending more inside the estuary compared with the modeled shoal area near SBN1 (Figure 6f). A comparison between modeled (SBN1, $t = 300$ years) and measured (in the year 1800 before closure of the secondary basins) hypsometries of the Western Scheldt Estuary (i.e., bathymetric surface area located below a specific bed level z_b) also shows that the shoal surface area in 1800 was larger than that obtained from model results. The underestimation of shoal surface area by the model might be due to smaller initial amount of sediment available in the Western Scheldt Estuary compared with observations. Due to lack of availability of historical bed level data in the entire model domain (including Sea Scheldt and North Sea, Figure 2), the initial flat bed level used in the model simulations was based on presently measured bathymetry. However, the Western Scheldt Estuary in 1800 was generally shallower than at present, implying that the model underestimates sediment availability in this estuary. The study by Van der Wegen and Roelvink (2012) revealed that a shallower initial bathymetry of an estuary, and thus an initially larger amount of available sediment, leads to development of a larger shoal surface area compared with a deeper estuary.

5.2.2. Relevance of Model Results

The physical mechanism underlying the difference in channel location between cases with and without a secondary basin is that in the former case, weaker and more eccentric tidal currents form in the main estuary near the secondary basin, favoring sediment deposition and shoal development in this area. Weakening of tidal currents in the main estuary for an arbitrary location of a SB was also obtained from the one-dimensional network model of Alebregtse and de Swart (2014) for a prismatic estuary (i.e., constant width and depth) in the case of moderate to high bottom friction. Kumar et al. (2014), who used a three-dimensional model to investigate the influence of secondary basins on the tidal and sediment dynamics in the Ems Estuary (Figure 1) reported the formation of a sediment convergence zone near these secondary basins. Furthermore, the modeling study by Li et al. (2016) revealed that besides the role of friction, reduction of tidal amplitude is larger for stronger converging estuaries. Specifically, their model results showed that in estuaries with moderate to high friction and converging planforms, there is always a weakening of the tidal amplitude, regardless of the location and shape of the SB. Alebregtse and de Swart (2014) found that changes occurring in the tidal amplitude due to the presence of a SB translate to similar changes in velocity, indicating that outcomes from the study by Li et al. (2016) apply for tidal currents as well. Based on the findings from these studies, sediment convergence, and consequently shoal development near secondary basins, is expected to particularly occur in estuaries with moderate to high friction and converging planforms. The latter statement is further supported by results from a recent analysis of a data set with 25 estuaries by Leuven et al. (2017), from which it appeared that larger shoals form at locations where the estuary is wider or secondary basins are present. Figure S6 in supporting information shows some examples of these estuaries, where shoals and tidal flats exist near their secondary basins. Results from the present study suggest that closure of secondary basins in this type of estuaries would result in a lateral displacement of the nearby channel toward the bank.

6. Conclusions

Model results show that significant spatial differences exist between channel network configurations obtained in cases without and with a secondary basin, particularly when the basin is located in areas of strong estuary bends. Some channels that appear in the case without a secondary basin are narrower or they do not exist in the case with basin. Moreover, channels that form in the vicinity of a secondary basin are located farther away from the bank of the estuary with respect to their positions in case without basin (channel location difference). Channel networks that form in areas of strong bends in the estuary are more sensitive to the presence of a secondary basin compared with those that form in areas of weak bends. Generally, in areas where the estuary strongly curves, the formation of a two-channel (single channel) network occurs if a secondary basin is located on the northern (southern) side of the estuary. Results obtained with two secondary basins are similar to those with a single basin, meaning that channel location difference exists near each of the two basins. In case with three secondary basins, however, channel location difference appears only near one basin. Regarding the geometry of the secondary basin, it turns out that channel location difference is determined by the width of the basin. The wider the basin, the farther away the nearby channel forms.

If a secondary basin is removed from the estuary, the nearby channel starts to migrate toward the bank of the estuary where the basin was located. Modeled timescales of channel displacement (order decades to centuries) seem to be consistent with observations. These results provide support for the hypothesis that closure of secondary basins Sloe, Braakman, and Hellegat in the Western Scheldt is responsible for the observed channel migration toward the bank of the estuary. A significant difference between model results and observations, however, is that the computed lateral displacement of the channel is much smaller than the observed channel displacement in the Western Scheldt over the last two centuries.

The physical mechanism is that the presence of a secondary basin causes weaker and more eccentric (rotary) tidal currents in the main estuary near the basin, such that sediment is deposited in this area. Consequently, a shoal grows, which eventually causes the main channel to form farther away from the bank of the estuary compared with the case without a secondary basin. If a secondary basin is removed from the estuary, the margin of the nearby channel starts to erode due to stronger and more bidirectional tidal currents in this area, resulting in channel migration toward the bank of the estuary. This physical mechanism is expected to particularly apply for estuaries with moderate to high friction and converging width.

Finally, as openings of new secondary basins have gained increasing popularity among coastal managers to reduce tidal range and turbidity, outcomes from this study suggest that particularly in the cases of estuaries with moderate to high friction, the presence of these new basins will result in an off-bank lateral displacement of the nearby channels.

Appendix A: Expressions Net Sediment Components

The components of net sediment transport are given by the following expressions.

$$\begin{aligned} T_{1x} &= \frac{1}{8}u_o\left[15\hat{u}_2^4 + 3\hat{v}_2^4 + 12\hat{u}_2^2\hat{v}_2^2\left(1+\frac{1}{2}\cos\left[2\left(\phi_2-\psi_2\right)\right]\right)\right] \\ &\quad + \frac{3}{2}v_o\cos\left[\phi_2-\psi_2\right]\left[\hat{u}_2^3\hat{v}_2 + \hat{u}_2\hat{v}_2^3\right], \\ T_{1y} &= \frac{1}{8}v_o\left[15\hat{v}_2^4 + 3\hat{u}_2^4 + 12\hat{u}_2^2\hat{v}_2^2\left(1+\frac{1}{2}\cos\left[2\left(\phi_2-\psi_2\right)\right]\right)\right] \\ &\quad + \frac{3}{2}u_o\cos\left[\phi_2-\psi_2\right]\left[\hat{u}_2^3\hat{v}_2 + \hat{u}_2\hat{v}_2^3\right], \end{aligned} \tag{A1}$$

$$\begin{aligned} T_{2x} &= \frac{1}{4}\hat{u}_4\left[5\hat{u}_2^4\cos\left[2\phi_2-\phi_4\right] + 6\hat{u}_2^2\hat{v}_2^2\cos\left[\phi_2-\psi_2\right]\cos\left[\phi_2+\psi_2-\phi_4\right] + \hat{v}_2^4\cos\left[2\psi_2-\phi_4\right]\right] \\ &\quad + \frac{1}{4}\hat{v}_4\left[\hat{u}_2^3v_2\left(3\cos\left[\phi_2+\psi_2-\psi_4\right] + \cos\left[3\phi_2-\psi_2-\psi_4\right]\right)\right. \\ &\quad \left.+\hat{u}_2\hat{v}_2^3\left(3\cos\left[\phi_2+\psi_2-\psi_4\right] + \cos\left[\phi_2-3\psi_2+\psi_4\right]\right)\right], \\ T_{2y} &= \frac{1}{4}v_4\left[5\hat{v}_2^4\cos\left[2\psi_2-\psi_4\right] + 6\hat{u}_2^2\hat{v}_2^2\cos\left[\phi_2-\psi_2\right]\cos\left[\phi_2+\psi_2-\psi_4\right] + \hat{u}_2^4\cos\left[2\phi_2-\psi_4\right]\right] \\ &\quad + \frac{1}{4}\hat{u}_4\left[\hat{u}_2^3\hat{v}_2\left(3\cos\left[\phi_2+\psi_2-\phi_4\right] + \cos\left[3\phi_2-\psi_2-\phi_4\right]\right)\right. \\ &\quad \left.+\hat{u}_2\hat{v}_2^3\left(3\cos\left[\phi_2+\psi_2-\phi_4\right] + \cos\left[\phi_2-3\psi_2+\phi_4\right]\right)\right]. \end{aligned} \tag{A2}$$

Acknowledgments

We would like to express our sincere gratitude to Huib de Swart (IMAU, Utrecht University, The Netherlands) who provided insight and expertise that greatly assisted this research. Also, we are grateful for his detailed and constructive feedback that greatly improved the manuscript. Rijkswaterstaat (Ministry of Infrastructure and the Environment, The Netherlands) is acknowledged for providing historical bathymetric data of the Western Scheldt Estuary and making their water levels and velocities data publicly accessible. Finally, we would like to thank Gerard Dam (Svasek Hydraulics, The Netherlands) for providing other historical bathymetric data of the Western Scheldt Estuary. This research is part of project "Agenda voor de Toekomst," 14_094, which is funded by the Flemish-Dutch Scheldt Commission (Vlaams-Nederlandse Scheldecommissie, VNSC). Historical bathymetric data of study area and model output data can be accessed on https://figshare.com/s/20c06b2d0e2b94717ab3.

References

Alebregtse, N., & de Swart, H. (2014). Effect of a secondary channel on the non-linear tidal dynamics in a semi-enclosed channel: A simple model. *Ocean dynamics*, *64*(4), 573–585.

Alebregtse, N. C., De Swart, H., & Schuttelaars, H. (2013). Resonance characteristics of tides in branching channels. *Journal of fluid mechanics*, *728*, R3.

Archambault, P., McKindsey, C., & Bourget, E. (1999). Large-scale shoreline configuration influences phytoplankton concentration and mussel growth. *Estuarine, Coastal and Shelf Science*, *49*(2), 193–208. https://doi.org/10.1006/ecss.1999.0481

Canestrelli, A., Lanzoni, S., & Fagherazzi, S. (2013). One-dimensional numerical modeling of the long-term morphodynamic evolution of a tidally-dominated estuary: The lower Fly River (Papua New Guinea). *Sedimentary Geology*, *301*, 107–119. https://doi.org/10.1016/j.sedgeo.2013.06.009

Chu, K., Winter, C., Hebbeln, D., & Schulz, M. (2011). Optimization scheme for coastal morphodynamic model. *Journal of Coastal Research*, *64*, 736–740.

Dabrio, C. J., Zazo, C., Goy, J. L., Sierro, F. J., Borja, F., Lario, J., … Flores, J. A. (2000). Depositional history of estuarine infill during the last postglacial transgression (Gulf of Cadiz, Southern Spain). *Marine Geology*, *162*(2), 381–404. https://doi.org/10.1016/S0025-3227(99)00069-9

Dalrymple, R. W., Zaitlin, B. A., & Boyd, R. (1992). Estuarine facies models: Conceptual basis and stratigraphic implications: Perspective. *Journal of Sedimentary Research*, *62*(6), 1130–1146.

Dam, G., Wegen, M., Labeur, R., & Roelvink, D. (2016). Modeling centuries of estuarine morphodynamics in the Western Scheldt Estuary. *Geophysical Research Letters*, *43*, 3839–3847. https://doi.org/10.1002/2015GL066725

Deltares (2016). User manual Delft3d-Flow: Simulation of multi-dimensional hydrodynamic flows and transport phenomena, including sediments (Tech. Rep.) Version 3.15, Delft, The Netherlands.

Donner, M., Ladage, F., Stoschek, O., & Nguyen, H. H. (2012). Methods and analysis tools for redevelopments in an estuary with high suspended sediment concentrations. *Coastal Engineering Proceedings*, *1*(33), 55.

Eelkema, M. (2013). Eastern Scheldt inlet morphodynamics (PhD thesis). Delft University of Technology, TU Delft.

Engelund, E., & Hansen, E. (1967). A monograph on sediment transport in alluvial streams (Tech. Rep.) Copenhagen, Denmark: Teknisk Forlag.

Fletcher, C. A., & Spencer, T. (2005). *Flooding and environmental challenges for Venice and its lagoon: State of knowledge*. Cambridge, UK: Cambridge University Press.

Fletcher, C. H., Knebel, H. J., & Kraft, J. C. (1992). Holocene depocenter migration and sediment accumulation in Delaware Bay: A submerging marginal marine sedimentary basin. *Marine Geology*, *103*(1–3), 165–183. https://doi.org/10.1016/0025-3227(92)90014-9

French, P. (2002). *Coastal and estuarine management* (p. 251). London: Routledge.

Garnier, R., Calvete, D., Falqués, A., & Caballeria, M. (2006). Generation and nonlinear evolution of shore-oblique/transverse sand bars. *Journal of Fluid Mechanics*, *567*, 327–360. https://doi.org/10.1017/S0022112006002126

Healy, M., & Hickey, K. R. (2002). Historic land reclamation in the intertidal wetlands of the Shannon Estuary, western Ireland. In *The 7th International Coastal Symposium, ICS 2002*, Coastal Education and Research Foundation (CERF), Northern Ireland.

Hibma, A., Schuttelaars, H. M., & Wang, Z. B. (2003). Comparison of longitudinal equilibrium profiles of estuaries in idealized and process-based models. *Ocean Dynamics*, *53*(3), 252–269. https://doi.org/10.1007/s10236-003-0046-7

Jaffe, B. E., Smith, R. E., & Foxgrover, A. C. (2007). Anthropogenic influence on sedimentation and intertidal mudflat change in San Pablo Bay, California: 1856–1983. *Estuarine, Coastal and Shelf Science*, *73*(1), 175–187. https://doi.org/10.1016/j.ecss.2007.02.017

Jeuken, M. (2000). On the morphological behaviour of tidal channels in the Westerschelde Estuary (PhD thesis). The Netherlands.

Jeuken, M., & Wang, Z. (2010). Impact of dredging and dumping on the stability of ebb-flood channel systems. *Coastal Engineering*, *57*(2010), 553–566. https://doi.org/10.1016/j.Coastaleng.2009.12.004

Kalkwijk, J. T., & De Vriend, H. J. (1980). Computation of the flow in shallow river bends. *Journal of Hydraulic Research*, *18*(4), 327–342.

Kuijper, C., Steijn, R., Roelvink, J., Kaaij, T., & Olijslagers, P. (2004). Morphological modelling of the Western Scheldt: Validation of DELFT3D (Tech. Rep.) Deltares (WL).

Kumar, M., Schuttelaars, H. M., & Roos, P. C. (2014). Understanding the influence of retention basin on tidal dynamics in tidal estuaries. In *Proceedings of the 17th Physics of Estuaries and Coastal Seas (PECS) Conference* (Vol. 16, pp. 14254). Porto de Galinhas, Pernambuco, Brazil.

Latteux, B. (1995). Techniques for long-term morphological simulation under tidal action. *Marine Geology*, *126*(1–4), 129–141. https://doi.org/10.1016/0025-3227(95)00069-B

Lesser, G., Roelvink, J., Van Kester, J., & Stelling, G. (2004). Development and validation of a three-dimensional morphological model. *Coastal Engineering*, *51*(8), 883–915. https://doi.org/10.1016/j.coastaleng.2004.07.014

Leuven, J., Haas, T., Braat, L., & Kleinhans, M. (2017). Topographic forcing of tidal sand bar patterns for irregular estuary planforms. *Earth Surface Processes and Landforms*, *43*(1), 172–186. https://doi.org/10.1002/esp.4166

Li, C., Schuttelaars, H. M., Roos, P. C., Damveld, J. H., Gong, W., & Hulscher, S. J. (2016). Influence of retention basins on tidal dynamics in estuaries: Application to the Ems Estuary. *Ocean & Coastal Management*, *134*, 216–225. https://doi.org/10.1016/j.ocecoaman.2016.10.010

Madsen, A. T., Murray, A., Andersen, T. J., & Pejrup, M. (2007). Temporal changes of accretion rates on an estuarine salt marsh during the late Holocene reflection of local sea level changes? The Wadden Sea, Denmark. *Marine Geology*, *242*(4), 221–233. https://doi.org/10.1016/j.margeo.2007.03.001

Morris, J. T., Sundareshwar, P., Nietch, C. T., Kjerfve, B., & Cahoon, D. R. (2002). Responses of coastal wetlands to rising sea level. *Ecology*, *83*(10), 2869–2877.

Nnafie, A., de Swart, H. E., Garnier, R., & Calvete, D. (2014). Modeling the response of shoreface-connected sand ridges to sand extraction on an inner shelf. *Ocean Dynamics*, *SC*, 1–18. https://doi.org/10. 1007/s10236-014-0714-9

Okubo, A. (1973). Effect of shoreline irregularities on streamwise dispersion in estuaries and other embayments. *Netherlands Journal of Sea Research*, *6*(1–2), 213–224. https://doi.org/10.1016/0077-7579(73) 90014-8

Perillo, G. M. (1995). Geomorphology and sedimentology of estuaries: An introduction. *Developments in Sedimentology*, *53*, 1–16. https://doi.org/10.1016/S0070-4571(05)80021-4

Pierik, H., Cohen, K., Vos, P., van der Spek, A., & Stouthamer, E. (2017). Late Holocene coastal-plain evolution of the Netherlands: The role of natural preconditions in human-induced sea ingressions. *Proceedings of the Geologists' Association*, *128*(2), 180–197. https://doi.org/10.1016/j.pgeola.2016.12.002

Pye, K., & Blott, S. J. (2014). The geomorphology of UK estuaries: The role of geological controls, antecedent conditions and human activities. *Estuarine, Coastal and Shelf Science*, *150*, 196–214. https://doi.org/10.1016/j.ecss.2014.05.014

Roelvink, J. (2006). Coastal morphodynamic evolution techniques. *Coastal Engineering*, *53*(2), 277–287. https://doi.org/10.1016/j.coastaleng.2005.10.015

Roelvink, J., & Walstra, D.-J. (2004). Keeping it simple by using complex models. *Advances in Hydro-science and Engineering*, *6*, 1–11.

Roos, P. C., & Schuttelaars, H. M. (2015). Resonance properties of tidal channels with multiple retention basins: Role of adjacent sea. *Ocean dynamics*, *65*(3), 311–324. https://doi.org/10.1007/s10236-015-0809-y

Rossi, V., Amorosi, A., Sarti, G., & Potenza, M. (2011). Influence of inherited topography on the Holocene sedimentary evolution of coastal systems: An example from Arno coastal plain (Tuscany, Italy). *Geomorphology*, *135*(1), 117–128. https://doi.org/10.1016/j.geomorph.2011.08.009

Schubel, J., & Pritchard, D. (1972). The estuarine environment, Part 1. *Journal of Geological Education*, *20*(2), 60–68.

Sherwood, C. R., Jay, D. A., Harvey, R. B., Hamilton, P., & Simenstad, C. A. (1990). Historical changes in the Columbia River estuary. *Progress in Oceanography*, *25*(1–4), 299–352. https://doi.org/10.1016/0079-6611(90) 90011-P

Syvitski, J. P., Kettner, A. J., Overeem, I., Hutton, E. W., Hannon, M. T., Brakenridge, G. R., … Nicholls, R. J. (2009). Sinking deltas due to human activities. *Nature Geoscience*, *2*(10), 681–686. https://doi.org/10.1038/ngeo629

Törnqvist, T. E., Wallace, D. J., Storms, J. E., Wallinga, J., Van Dam, R. L., Blaauw, M., … Snijders, E. M. (2008). Mississippi delta subsidence primarily caused by compaction of Holocene strata. *Nature Geoscience*, *1*(3), 173—176. https://doi.org/10.1038/ngeo129

Van de Kreeke, J., & Robaczewska, K. (1993). Tide-induced residual transport of coarse sediment; application to the Ems Estuary. *Netherlands Journal of Sea Research*, *31*(3), 209–220.

Van der Spek, A. (1997). Tidal asymmetry and long-term evolution of Holocene tidal basins in The Netherlands: Simulation of palaeo-tides in the Schelde Estuary. *Marine Geology*, *141*(1), 71–90. https://doi.org/10.1016/S0025-3227(97)00064-9

Van der Wegen, M., & Roelvink, J. (2008). Long-term morphodynamic evolution of a tidal embayment using a two-dimensional, process-based model. *Journal of Geophysical Research*, *113*, C03016. https://doi.org/10.1029/2006JC003983

Van der Wegen, M., & Roelvink, J. (2012). Reproduction of estuarine bathymetry by means of a process-based model: Western Scheldt case study, the Netherlands. *Geomorphology*, *179*, 152–167. https://doi.org/10.1016/j.geomorph.2012. 08.007

Van Maren, D., Oost, A., Wang, Z., & Vos, P. (2016). The effect of land reclamations and sediment extraction on the suspended sediment concentration in the Ems Estuary. *Marine Geology*, *376*, 147–157. https://doi.org/10.1016/j.margeo.2016.03.007

Van Rijn, L. (2007). Unified view of sediment transport by currents and waves. I: Initiation of motion, bed roughness, and bed-load transport. *Journal of Hydraulic Engineering*, *133*, 649–6671. https://doi.org/10.1061/(ASCE) 0733-9429(2007)133:6(649)

van Rijn, L. C. (2011). Analytical and numerical analysis of tides and salinities in estuaries; part I: Tidal wave propagation in convergent estuaries. *Ocean Dynamics*, *61*(11), 1719–1741. https://doi.org/10.1007/s10236-011-0453-0

Van Veen, J. (1950). Eb en vloed scharen in de Nederlandsche getij wateren. *Journal of the Royal Dutch Geographical Society (KNAG)*, *67*, 303–325. English translation, Delft University Press, Delft, the Netherlands, 2002.

Wahl, T., Haigh, I., Woodworth, P. L., Albrecht, F., Dillingh, D., Jensen, J., … Wöppelmann, G. (2013). Observed mean sea level changes around the North Sea coastline from 1800 to present. *Earth-Science Reviews*, *124*, 51–67. https://doi.org/10.1016/j.earscirev.2013.05.003

Wang, Z., Jeuken, M., Gerritsen, H., De Vriend, H., & Kornman, B. (2002). Morphology and asymmetry of the vertical tide in the Westerschelde Estuary. *Continental Shelf Research*, *22*(17), 2599–2609. https://doi.org/10.1016/S0278-4343(02)00134-6

Woodruff, J. D., Martini, A. P., Elzidani, E. Z., Naughton, T. J., Kekacs, D. J., & MacDonald, D. G. (2013). Off-river water bodies on tidal rivers: Human impact on rates of infilling and the accumulation of pollutants. *Geomorphology*, *184*, 38–50.

Yellen, B., Woodruff, J. D., Ralston, D. K., MacDonald, D. G., & Jones, D. S. (2017). Salt wedge dynamics lead to enhanced sediment trapping within side embayments in high-energy estuaries. *Journal of Geophysical Research: Oceans*, *122*, 2226–2242. https://doi.org/10.1002/2016JC012595

Zeinali, S., Talebbeydokhti, N., Jandaghian, M., & Tavakkol, S. (2014). Coastal morph dynamics and long-term morphological modeling: A review. *Research Journal of Environmental and Earth Sciences*, *6*(11), 493–499.

Zitman, T. J. (1999). Getijanalyse Westerschelde (Tidal analysis Western Scheldt) (Tech. Rep.) The Netherlands. Report in Dutch.